

# Role of Ni<sup>2+</sup> Ions in Magnetite Nano-particles Synthesized by Co-precipitation Method

Safia Anjum<sup>1</sup> · Hafsa Saleem<sup>1</sup> · Khalid Rasheed<sup>2</sup> · Rehana Zia<sup>1</sup> · Saira Riaz<sup>3</sup> · Arslan Usman<sup>4</sup>

Received: 5 July 2016 / Accepted: 13 August 2016 / Published online: 19 November 2016  
© Springer Science+Business Media New York 2016

**Abstract** In the present work, nickel-doped iron oxide (Ni<sub>x</sub>Fe<sub>3-x</sub>O<sub>4</sub>) nanoparticles with different concentration of nickel ( $x = 0, 0.05, 0.1, \text{ and } 0.15$ ) have been prepared by co-precipitation method. These prepared nanoparticles have been characterized by using x-ray diffractometer, thermo gravimetric analysis and differential scanning calorimetry, Fourier transform infrared spectroscopy, scanning electron microscopy, vibrating sample magnetometer, and UV-Visible spectroscopy to study their structural, thermal, morphological, magnetic, and optical properties, respectively. The x-ray diffraction confirms the formation of single-phase inverse spinel cubic structure of NiFe<sub>3</sub>O<sub>4</sub> nanoparticles. Crystallite size has been estimated by the full width at half maximum of the most intense x-ray diffraction peak where vibrational and stretching modes of metal-oxygen bonds in 872 cm are shown in Fourier transform infrared spectra which confirms the formation of nanoparticles. The thermal analysis revealed that the transition temperature and stability increases with increasing

Ni concentration. The surface morphology indicated that the particles are spherical in shape with some agglomeration. The magnetic measurement revealed that the coercivity and anisotropy increases with nickel doping in magnetite nanoparticles. The optical analysis revealed that direct and indirect both types of band gap increases when the particle size decreases because the absorption spectra shift toward smaller wavelength. The blue shift confirms the formation of nanoparticles.

**Keywords** Nanoparticles · Stability · Magnetic properties · Magnetic materials · Anisotropy · Optical properties · Co-precipitation

## 1 Introduction

Magnetic particle sizes from nanometer to micrometer are attractive materials not only in the field of magnetic recording but also in areas of biological and medical applications. One of the promising particles is the iron oxide nanoparticle of various kinds and its derivatives [1]. Magnetite (Fe<sub>3</sub>O<sub>4</sub>) is one of the most important magnetic materials because it is widely used as materials for drug carriers [2], drug release, cancer therapy [3], hyperthermia [4], magnetic separation, magnetic resonance imaging [5], proton exchange membrane, and sensor [6]. However, magnetite nanoparticles are the most studied materials due to their response to magnetic field through the super paramagnetic behavior at room temperature with high-saturation magnetization. In addition, their non-toxicity and high biocompatibility are also suitable for biotechnology areas [7]. In order to tune the

✉ Safia Anjum  
safia.anjum@hotmail.com

<sup>1</sup> Department of Physics, Lahore College for Women University, Lahore, Pakistan

<sup>2</sup> PCSIR Laboratories Lahore, Lahore, Pakistan

<sup>3</sup> Centre for Solid State Physics, University of the Punjab, Lahore, Pakistan

<sup>4</sup> Department of Physics, COMSAT Institute of Information and Technology, Lahore, Pakistan

properties of magnetite nanoparticles, nickel is doped with different concentrations in magnetite nanoparticles.

Nano-sized nickel-doped iron oxide ( $\text{NiFe}_3\text{O}_4$ ) nanoparticles is one of the versatile and scientifically important soft ferrite material because of its distinctive ferromagnetic properties, e.g., low conductivity and hence lower eddy current losses [8], catalytic behavior [9], high electrochemical stability abundance in nature, etc. Nickel-doped iron oxide ( $\text{Ni}_x\text{Fe}_{3-x}\text{O}_4$ ) nanoparticles have inverse spinel structure in which eight units of nickel ferrite ( $\text{Ni}_x\text{Fe}_{3-x}\text{O}_4$ ) form a unit cell of the spinel structure. Half of the ferric ions fill the tetrahedral sites (A sites) and the remaining half fill the octahedral site and nickel ions occupy the octahedral sites (B sites) [10]. Hence, the compound can be represented by the following formula:



There are various methods that are used for the fabrication of nanoparticles but the wet methods produced the best quality of nanoparticles, for example, co-precipitation, sol-gel, hydrothermal, and others [11]. The main purpose is to fabricate low-cost, homogeneous, and highly pure powders that have a very fine and small particle sizes with small agglomeration. In the present research, co-precipitation method is used for the synthesis of Ni-doped iron oxide nanoparticles because it is simple and efficient and has the capability to control the size [12], composition, and even the shape of the nanoparticles. The main advantage of this method is that the crystal structure is easily achieved without any heat treatment [13].

## 2 Experimental Setup

The chemicals used in the synthesis of magnetite and nickel-doped magnetite nanoparticles are ferrous chloride ( $\text{FeCl}_2$ ), ferric chloride ( $\text{FeCl}_3$ ), nickel chloride hexahydrate ( $\text{NiCl}_2 \cdot 6\text{H}_2\text{O}$ ), sodium hydroxide ( $\text{NaOH}$ ), and distilled water. The ( $\text{Ni}_x\text{Fe}_{3-x}\text{O}_4$ ) nanoparticles with different nickel concentration ( $x = 0, 0.05, 0.1, 0.15$ ) are prepared by co-

precipitation method. First of all, measure stoichiometric amounts of all chemicals by using the electronic balance. The molar mass of all chemicals is given in Table 1.

### 2.1 Synthesis Procedure

The nickel doped iron nano-particles have been prepared using take 1.2 g of ferrous chloride ( $\text{FeCl}_2$ ), 2.7 g of ferric chloride ( $\text{FeCl}_3$ ), and 0.1 g of nickel chloride in a beaker and dissolve in 100 ml of distilled water. Shake the beaker until all the chemicals have been completely dissolved in distilled water by co-precipitation method. Shake the beaker until all the chemicals have been completely dissolved in distilled water. After that took 1.6 g of sodium hydroxide ( $\text{NaOH}$ ) in a beaker and dissolved it in distilled water. Took the solution of  $\text{NaOH}$  in a burette and then added drop wise in the combined solution of ferrous, ferric, and nickel chloride. The combined solution of salts were constantly stirred using a magnetic stirrer and measured the temperature. Black precipitates were formed when the solution of sodium hydroxide ( $\text{NaOH}$ ) dropped into the combine solution of  $\text{Fe}^{2+}$ ,  $\text{Fe}^{3+}$ , and  $\text{Ni}^{2+}$ . The black precipitate indicated the formation of nickel doped iron oxide nanoparticles ( $\text{Ni}_x\text{Fe}_{3-x}\text{O}_4$ ) nanoparticles. The pH of the solution was measured by pH paper. The final product was washed with distilled water to removed unwanted impurities. The particles were dried in an oven at above  $100^\circ\text{C}$  for 24 h. The block diagram of co-precipitation method is shown in Fig. 1.

### 2.2 Characterization Techniques

A series of four samples of nickel-doped iron oxide ( $\text{Ni}_x\text{Fe}_{3-x}\text{O}_4$ ) nanoparticles with different nickel concentrations ( $x = 0, 0.05, 0.1, \text{ and } 0.15$ ) have been synthesized using chemical co-precipitation method. These prepared nanoparticles have been characterized using x-ray diffractometer (Model: PANalytical powder x-ray diffractometer with  $\text{Cu-K}\alpha\lambda = 0.154056 \text{ nm}$ ), Fourier transform infrared spectroscopy (Model: PerkinElmer FTIR spectrophotometer), differential scanning calorimetry, and thermo gravimetric analysis (Model: Mettler Toledo Ltd. Instrument) at heating rate of  $10^\circ\text{C}/\text{min}$  from room temperature to  $1000^\circ\text{C}$  in nitrogen atmosphere), scanning electron microscopy (Model: FEI Quanta FEG 200 (HR-SEM) equipments), vibrating sample magnetometer (VSM, Model Lakeshore 7400 and 7436) with an applied field of  $\pm 10 \text{ K Oe}$  and UV-Visible spectroscopy (Model: Perkin Emert Lambda spectrophotometer) to study their structural, thermal, morphological, magnetic, and optical properties, respectively. The 3-D structural view of  $\text{Ni}_x\text{Fe}_{3-x}\text{O}_4$  ( $x = 0, 0.05, 0.1, \text{ and } 0.15$ ) nanoparticles is made by using diamond software.

**Table 1** Molecular weights of all the chemicals

Materials	Chemical formula	Molecular weight (grams/mole)
Ferrous Chloride	$\text{FeCl}_2$	1.2
Ferric Chloride	$\text{FeCl}_3$	2.7
Nickel Chloride Hexahydrate	$\text{NiCl}_2 \cdot 6\text{H}_2\text{O}$	0.11
Sodium Hydroxide	$\text{NaOH}$	1.6

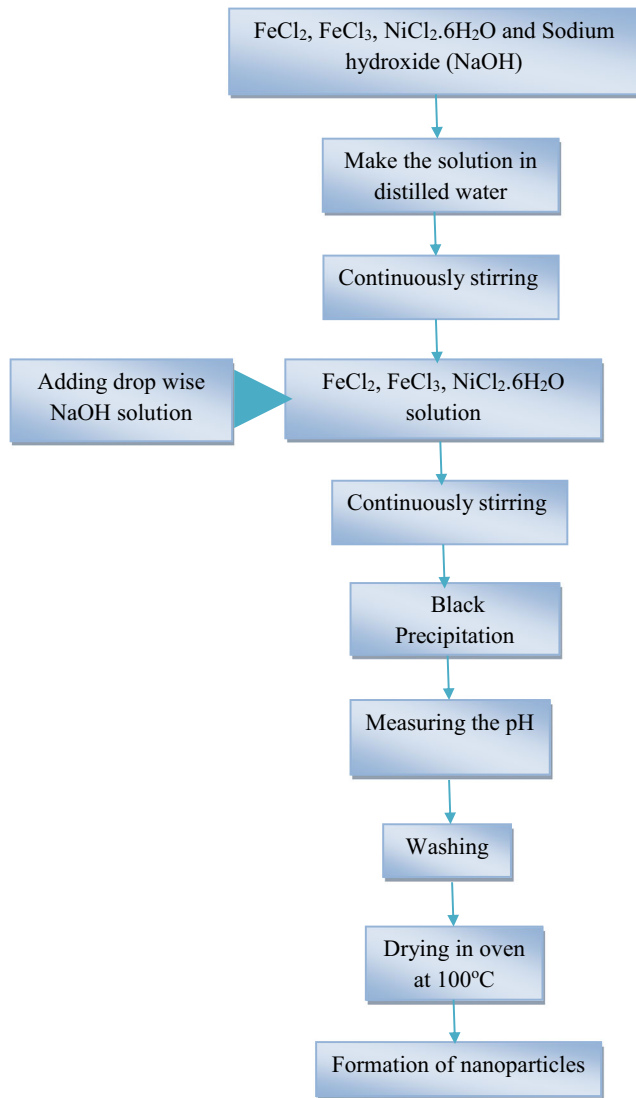


Fig. 1 Block diagram of co-precipitation method

### 3 Results and Discussions

#### 3.1 XRD Analysis

The XRD patterns of  $Ni_xFe_{3-x}O_4$  ( $x = 0, 0.05, 0.1, 0.15$ ) nanoparticles is shown in Fig. 2. The diffraction peaks are matched with the standard JCPDS card no. 19-0629 [14], which confirms the successful formation of single-phase cubic inverse spinel structure of iron oxide and nickel-doped iron oxide nanoparticles with the presence of (220), (311), (222), (400), (422), (511), and (440) planes.

In inverse spinel structure,  $Ni^{2+}$  ions preferably occupy the octahedral and  $Fe^{3+}$  ions equally distributed on both tetrahedral and octahedral sites as shown in the formula:

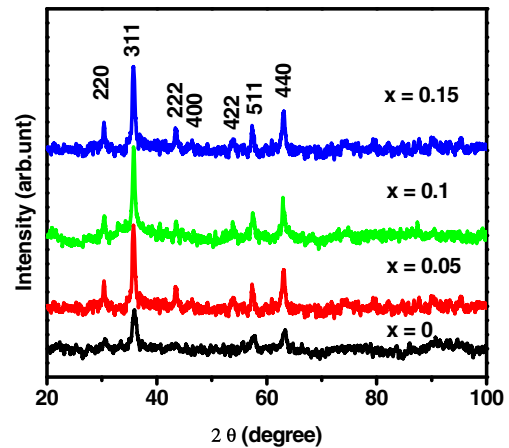
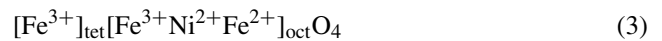


Fig. 2 XRD patterns of all the samples of  $Ni_xFe_{3-x}O_4$  nanoparticles

$Fe^{2+}$  ions have been successfully replaced by  $Ni^{2+}$  ions in octahedral site as shown in formula:



The structural parameters such as crystallite size, lattice parameters, and x-ray density have been evaluated from XRD patterns which are listed in Table 2. The crystallite size of synthesized iron oxide ( $Fe_3O_4$ ) and nickel-doped iron oxide ( $Ni_xFe_{3-x}O_4$ ) nanoparticles is calculated from the highest intense peak (311) using the Debye Scherrer's formula [15]:

$$D_p = \frac{0.94\lambda}{\beta \cos\theta} \quad (4)$$

where  $D_p$  is the crystallite size  $\beta$  is the full width at half maximum,  $\lambda$  is the wavelength of  $CuK\alpha$  radiation ( $\lambda = 1.54\text{\AA}$ ) and  $\theta$  is the Bragg angle. It is revealed that the crystallite size is decreased with increasing concentration of nickel as shown in Fig. 3. It is observed that the peaks of  $Ni_xFe_{3-x}O_4$  ( $x = 0, 0.05, 0.1, 0.15$ ) show broadening indicating the ultrafine nature of nanoparticles.

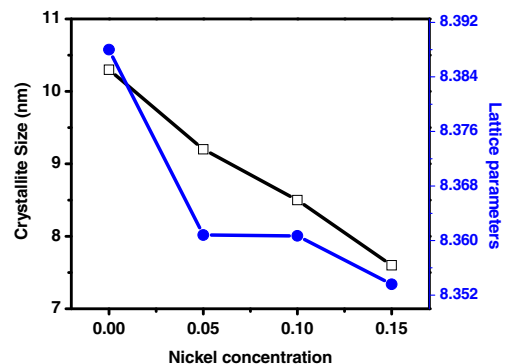


Fig. 3 Variation of crystallite size and Lattice parameters with Ni content

**Table 2** XRD data of  $\text{Ni}_x\text{Fe}_{3-x}\text{O}_4$  nanoparticles

Composition (x)	Position ( $2\theta$ )	FWHM (degree)	d-spacing ( $\text{Å}^\circ$ )	Crystallite size (nm)	Lattice parameters ( $\text{Å}^\circ$ )	X-ray density ( $\text{g}/\text{cm}^3$ )	$I_{220}/I_{440}$
$\text{Fe}_3\text{O}_4$	35.927	0.76859	2.4976	10.3	8.3880	5.2034	0.48
$\text{Ni}_{0.05}\text{Fe}_{2.95}\text{O}_4$	35.761	0.84357	2.5089	9.2	8.3608	5.2066	0.49
$\text{Ni}_{0.10}\text{Fe}_{2.9}\text{O}_4$	35.788	0.89509	2.5070	8.5	8.3607	5.2098	0.56
$\text{Ni}_{0.15}\text{Fe}_{2.85}\text{O}_4$	35.764	0.91297	2.5086	7.6	8.3536	5.2130	0.66

The value of lattice parameters for each sample is calculated using the following equation [16]:

$$a = [d(h^2 + k^2 + l^2)^{1/2}] \quad (5)$$

where ( $h, k, l$ ) are the miller indices of the most intense peak (311). The lattice parameter decreased linearly with the increasing amount of  $\text{Ni}^{2+}$  ions in magnetite ( $\text{Fe}_3\text{O}_4$ ) nanoparticles which are in accordance with Vegard's law. The decrease in lattice parameter is based on the ionic radii of  $\text{Ni}^{2+}$  ( $0.69\text{Å}^\circ$ ) which is smaller than the ionic radii of  $\text{Fe}^{2+}$  ( $0.77\text{Å}^\circ$ ) ions. The partial substitution of Ni ions with Fe ions in magnetite nanoparticles can cause the reduction of unit cell dimensions and therefore lattice parameters decrease.

X-ray density depends upon the lattice parameters, so it is calculated using the formula [17]:

$$dx = \frac{8M}{Na^3} \quad (6)$$

where 8 shows the number of molecules per unit cell of cubic spinel lattice,  $M$  stands for molecular weight,  $N$  is the Avogadro number ( $6.02214 \times 10^{23}$ ) and  $a$  shows the lattice parameter. The graph of x-ray density as a function of nickel concentration is shown in Fig. 4. In the present system, it is investigated that the x-ray density increases with increasing nickel contents. This is due to the variation in the atomic weights of iron and nickel. The atomic weight of  $\text{Ni}^{2+}$  ( $58.6934 \text{ g/mol}$ ) is higher than that of  $\text{Fe}^{2+}$

( $55.845 \text{ g/mol}$ ). The ratio of decrease of lattice parameter is less as compare to the ratio of increase of molecular weight.

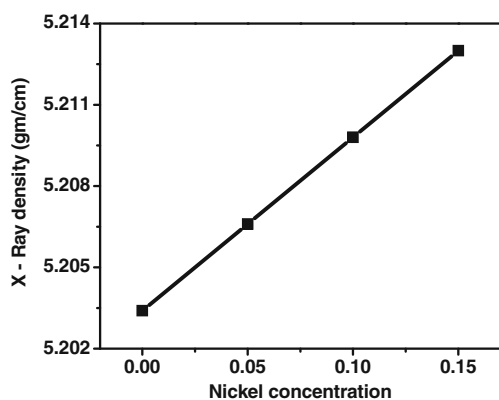
The cation distributions in tetrahedral and octahedral sites is explained on the basis of change in the intensities of the (2 2 0) and (4 4 0) planes. Table 2 demonstrate the change in the intensities of the (2 2 0) and (4 4 0) planes of  $\text{Ni}_x\text{Fe}_{3-x}\text{O}_4$  ( $x = 0, 0.05, 0.1, 0.15$ ) nanoparticles. It is observed in all the samples the intensity of (4 4 0) plane is larger as compare to (2 2 0) plane. The occupancy of nickel ions in octahedral site cause to decrease the intensity of (2 2 0) plane which depends upon the smaller ionic radius of Ni ions. The percentage of nickel in octahedral site depends on the ratio of  $I_{220}/I_{440}$  which is increased with increasing nickel concentration. This judgment confirms the formation of inverse spinel structure of  $\text{NiFe}_3\text{O}_4$  nanoparticles.

### 3.1.1 3-D Visualization

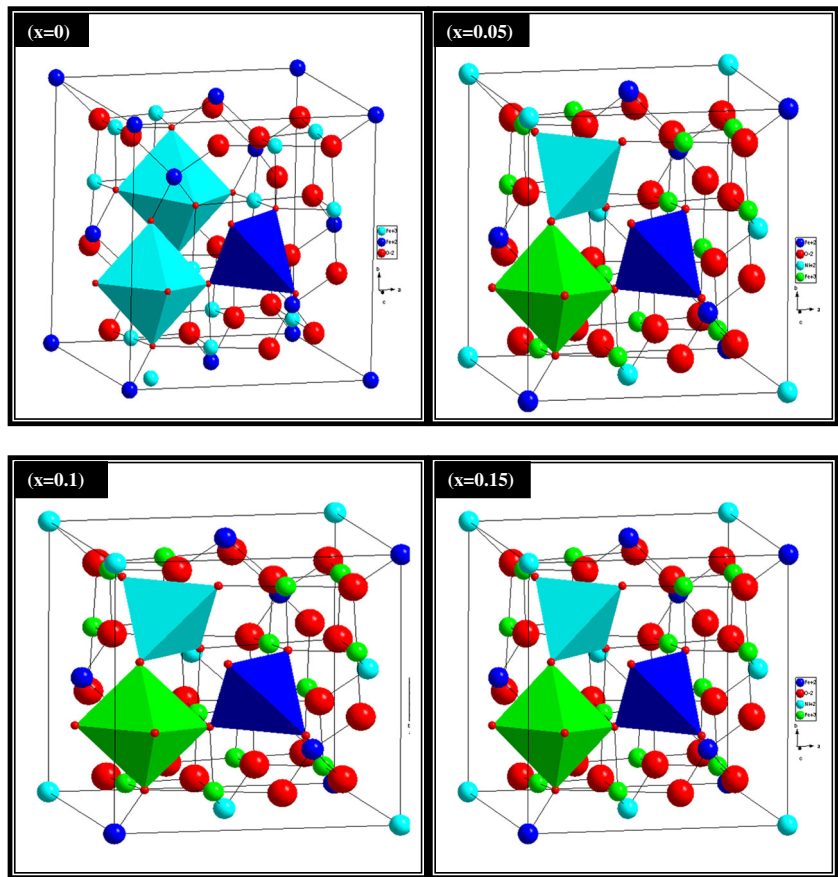
The 3-D visualization of  $\text{Ni}_x\text{Fe}_{3-x}\text{O}_4$  nanoparticles with different nickel concentrations ( $x = 0, 0.05, 0.1, 0.15$ ) is made by using diamond software and shown in Fig. 5a–d, respectively. The XRD study shows that the peaks are well matched with the spinel structure having Fd-3m (no. 227) space group. In the present case of  $\text{NiFe}_3\text{O}_4$  nanoparticles, all the ferric ions equally distributed on tetrahedral and octahedral sites and  $\text{Fe}^{2+}$  ions in octahedral site replace by  $\text{Ni}^{2+}$  ions. The Wyckoff sites and  $x, y,$  and  $z$  values of  $\text{Fe}_3\text{O}_4$  and  $\text{Ni}_x\text{Fe}_{3-x}\text{O}_4$  ( $x = 0.05, 0.1, 0.15$ ) nanoparticles are tabulated in Table 3.

### 3.2 FTIR Analysis

The types of bonds and functional groups in the prepared nanoparticles are determined by FTIR analysis. The FTIR spectra of  $\text{Ni}_x\text{Fe}_{3-x}\text{O}_4$  nanoparticles with ( $x = 0, 0.05, 0.1,$  and  $0.15$ ) have been recorded in wavelength range of ( $600\text{--}4000$ )  $\text{cm}^{-1}$ . The comparative spectra of  $\text{Ni}_x\text{Fe}_{3-x}\text{O}_4$  nanoparticles at different nickel concentration ( $x = 0, 0.05, 0.1,$  and  $0.15$ ) are shown in Fig. 6. The two M–O absorption bands in the range of  $780$  and  $870 \text{ cm}^{-1}$  confirms the formation of inverse spinel cubic structure of nanoparticles [18]. The absorption band O–H at  $1641 \text{ cm}^{-1}$  is ascribed due to the stretching vibration of the free or absorbed water molecules on sample surface. The band at  $1026 \text{ cm}^{-1}$  is

**Fig. 4** Variation of x-ray density with nickel content

**Fig. 5** 3-D structure of **a**  $\text{Fe}_3\text{O}_4$ , **b**  $\text{Ni}_{0.05}\text{Fe}_{2.95}\text{O}_4$ , **c**  $\text{Ni}_{0.1}\text{Fe}_{2.9}\text{O}_4$ , and **d**  $\text{Ni}_{0.15}\text{Fe}_{2.85}\text{O}_4$  nanoparticle



attributed due to the vibrational bond of C–O. This bond may be due to the  $\text{CO}_2$  in air. The peak at  $1430\text{ cm}^{-1}$  is due to the vibration of –CH bond. The peak observed in  $2355\text{ cm}^{-1}$  attributed due to the symmetric vibrations of –OH groups. This may be due to the use of KBr and distilled water in the sample preparation.

**3.3 DSC/TGA analysis**

Thermal investigation of as synthesized ( $\text{Ni}_x\text{Fe}_{3-x}\text{O}_4$ ) nanoparticles with ( $x = 0, 0.05, 0.1, \text{ and } 0.15$ ) are made to investigate the thermal stability of these nanoparticles. The analysis was performed in nitrogen atmosphere at  $10\text{ }^\circ\text{C}/\text{min}$  from  $100\text{ to }1200\text{ }^\circ\text{C}$ . The TGA curves of as-synthesized nanoparticles are shown in Fig. 7. The graph

shows the (%) weight loss with the change in temperature. As the temperature increases from  $30\text{ to }150\text{ }^\circ\text{C}$ , 2.0, 2.6, 2.5, and 2.2 % weight loss is observed in  $x = 0, 0.05, 0.1, \text{ and } 0.15$  samples, respectively, which is due to the loss of water molecule that are present on the surface of nanoparticles.

The variation in the values of heat flow as a function of temperature is shown in Fig. 8. The amount of energy

**Table 3** Atomic coordinates of  $\text{Ni}_x\text{Fe}_{3-x}\text{O}_4$  ( $x = 0, 0.05, 0.1, 0.15$ ) nanoparticles

Atom	Ox.	Wyck.	x	y	z
Fe	+2	16c	1/8	1/8	1/8
Fe	+3	16d	5/8	5/8	5/8
O	–2	32e	0.38672	0.38672	0.38672
Ni	+2	8b	1/2	1/2	1/2

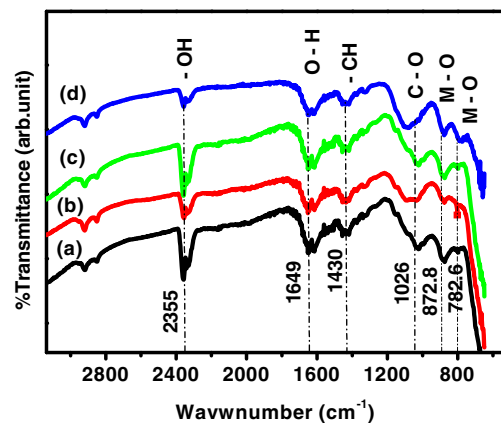


**Fig. 6** FTIR spectra of **a**  $\text{Fe}_3\text{O}_4$ , **b**  $\text{Ni}_{0.05}\text{Fe}_{2.95}\text{O}_4$ , **c**  $\text{Ni}_{0.1}\text{Fe}_{2.9}\text{O}_4$  and **d**  $\text{Ni}_{0.15}\text{Fe}_{2.85}\text{O}_4$  nanoparticles



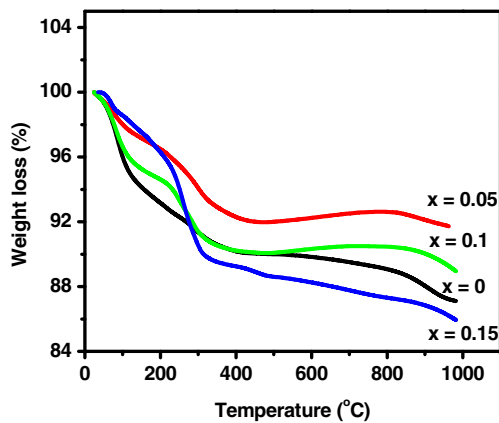


**Fig. 7** Variation in percent weight loss as a function of temperature of  $\text{Ni}_x\text{Fe}_{3-x}\text{O}_4$  nanoparticles (TGA curve)

released or absorbed ( $\Delta H$ ) during a phase transition is said to be enthalpy and determines the stability of the nanoparticles. The endothermic peak of all the samples was observed in the temperature range of 30–150 °C, which is due to the removal of moisture present in the sample. The enthalpy change is calculated using the formula [19]:

$$\Delta H = \frac{Q_2 - Q_1}{T_2 - T_1} \quad (7)$$

The enthalpy is calculated from the area under the exothermic peak. First, calculate the change in temperature ( $T_2 - T_1$ ) and then calculate change in heat ( $Q_2 - Q_1$ ) and put these values in the above-mentioned equation, this will give the value of enthalpy change.

A sharp exothermic peak is observed in magnetite nanoparticles at  $\sim 336$  °C temperature due to the phase transition from ( $\gamma\text{-Fe}_2\text{O}_3$  to  $\alpha\text{-Fe}_2\text{O}_3$ ). The peak starts at 207 °C and ends at 339 °C with an enthalpy change of  $-6.8$  J/g. When the concentration of nickel is increased, the value of enthalpy decreases from  $-15.8$  to  $-28.5$  J/g. In the present study, negative enthalpy is observed for all the

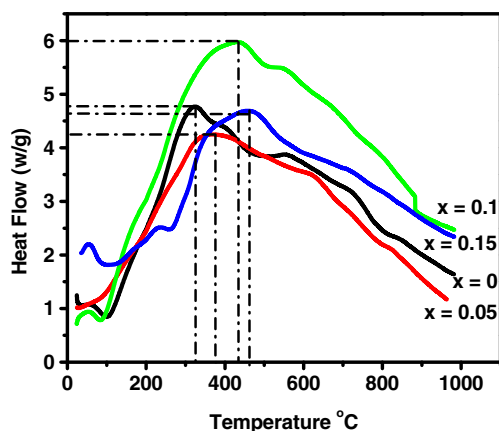


**Fig. 8** Variation in heat flow as a function of temperature of  $\text{Ni}_x\text{Fe}_{3-x}\text{O}_4$  nanoparticles (DSC curve)

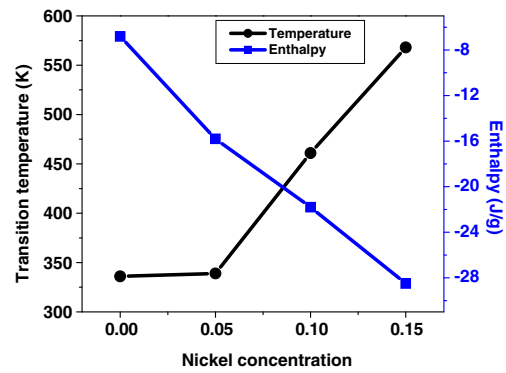


**Fig. 9** Variation in enthalpy and transition temperature as a function of nickel concentration

samples due to the phase transformation from maghemite to hematite. So, during the phase conversion from maghemite to hematite, the maximum energy is released from the system which gives rise to strong exothermic peaks in all the samples and increases the stability of nanoparticles. Fig. 9 shows the variation of transition temperature and enthalpy as a function of nickel concentration. It is revealed from the figure that when the concentration of nickel increases, the transition temperature increases and enthalpy decreases. The values of enthalpy change at different nickel concentrations are tabulated in Table 4.

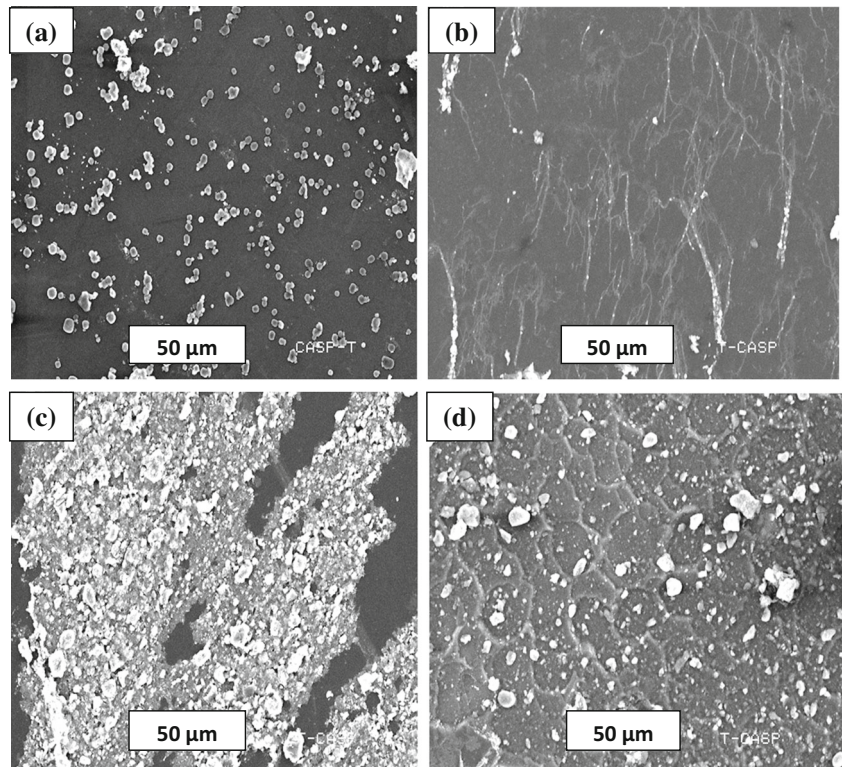
### 3.4 Surface Morphology

The morphology of prepared nanoparticles is determined by scanning electron microscopy (SEM). The sample was prepared by sonication. First of all, dissolved the powder samples in deionized water then put the sample in a sonicator for 30 min. After sonication, one drop of sonicated sample was placed on the shiny surface of silicon wafer and dried on a hot plate. The SEM micrographs of  $\text{Ni}_x\text{Fe}_{3-x}\text{O}_4$  ( $x = 0, 0.05, 0.1, \text{ and } 0.15$ ) nanoparticles at different resolutions are shown in Fig. 10. All the microstructures revealed the uniform and spherical shape of iron oxide and nickel-doped iron oxide nanoparticles. There is no agglomeration in iron oxide nanoparticles; however, when Ni is substituted in iron oxide nanoparticles with different concentrations ( $x = 0.05, 0.1, \text{ and } 0.15$ ), microstructures

**Table 4** Values of enthalpy and phase transition temperature of all the samples

Samples	Transition temperature °C	Enthalpy J/g
$\text{Fe}_3\text{O}_4$	336	-6.80
$\text{Ni}_{0.05}\text{Fe}_{2.95}\text{O}_4$	339	-15.8
$\text{Ni}_{0.10}\text{Fe}_{2.9}\text{O}_4$	461	-21.8
$\text{Ni}_{0.15}\text{Fe}_{2.85}\text{O}_4$	568	-28.5

**Fig. 10** SEM micrographs of **a**  $\text{Fe}_3\text{O}_4$ , **b**  $\text{Ni}_{0.05}\text{Fe}_{2.95}\text{O}_4$ , **c**  $\text{Ni}_{0.1}\text{Fe}_{2.9}\text{O}_4$ , and **d**  $\text{Ni}_{0.15}\text{Fe}_{2.85}\text{O}_4$  nanoparticles at 50- $\mu\text{m}$  resolution



have shown some agglomeration. The average particle size determined by SEM is listed in Table 5.

### 3.5 Magnetic Properties

Vibrating sample magnetometer (VSM) is used to describe the magnetic properties of  $\text{Ni}_x\text{Fe}_{3-x}\text{O}_4$  ( $x = 0, 0.05, 0.1, 0.15$ ) nanoparticles. The hysteresis loop of all the samples of  $\text{Ni}_x\text{Fe}_{3-x}\text{O}_4$  ( $x = 0, 0.05, 0.1, 0.15$ ) nanoparticles is shown in Fig. 11. The magnetic parameters such as saturation magnetization ( $M_s$ ), magnetic moment ( $n_B$ ), and coercivity ( $H_c$ ) are listed in Table 6.

It is observed that the saturation magnetization increases in 5 and 10 % nickel-doped magnetite nanoparticles and than it is decreased in 15 % Ni-doped nanoparticles. Magnetic properties are directly related to the distribution of the cations over tetrahedral and octahedral lattice sites.

**Table 5** Average particle size of all the samples calculated from SEM

Samples	Average particle size (nm)
$\text{Fe}_3\text{O}_4$	97.44
$\text{Ni}_{0.05}\text{Fe}_{2.95}\text{O}_4$	88.92
$\text{Ni}_{0.10}\text{Fe}_{2.9}\text{O}_4$	86.38
$\text{Ni}_{0.15}\text{Fe}_{2.85}\text{O}_4$	86

It is also revealed that the coercivity increases with increasing amount of nickel substitution as shown in Fig. 12. This is because of the decrease in crystallite size by the doping of nickel ions. The anisotropy constant  $K$  is calculated using the following the relation [20].

$$K = \frac{M_s \times H_c}{0.98} \tag{8}$$

Anisotropy constant  $K$  depends on the substituted ion concentration. This means that the anisotropy constant increases with increasing nickel content as shown in Fig. 13

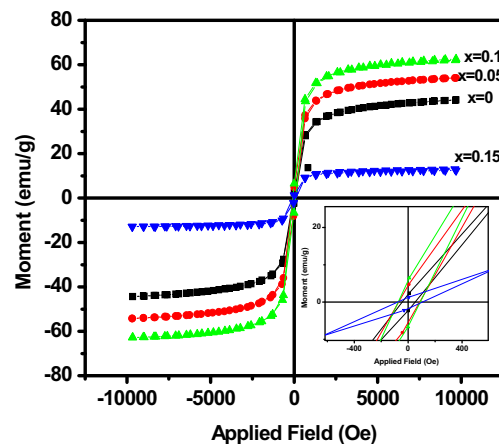


**Fig. 11** Hysteresis loops of **a**  $\text{Fe}_3\text{O}_4$ , **b**  $\text{Ni}_{0.05}\text{Fe}_{2.95}\text{O}_4$ , **c**  $\text{Ni}_{0.1}\text{Fe}_{2.9}\text{O}_4$ , and **d**  $\text{Ni}_{0.15}\text{Fe}_{2.85}\text{O}_4$  nanoparticles

**Table 6** Magnetic properties of  $\text{Ni}_x\text{Fe}_{3-x}\text{O}_4$  ( $x = 0, 0.05, 0.1, 0.15$ ) nanoparticles

Samples	Magnetization $M_s$ (emu/g)	Coercivity $H_c$ (Oe)	Magnetic moment $(n_B)$	Anisotropy $K$ (erg/g)
$\text{Fe}_3\text{O}_4$	44.11	54.08	1.82	2433
$\text{Ni}_{0.05}\text{Fe}_{2.95}\text{O}_4$	54.02	78.26	2.24	4310
$\text{Ni}_{0.10}\text{Fe}_{2.9}\text{O}_4$	62.81	97.42	2.60	6242
$\text{Ni}_{0.15}\text{Fe}_{2.85}\text{O}_4$	12.95	99.31	0.53	1312

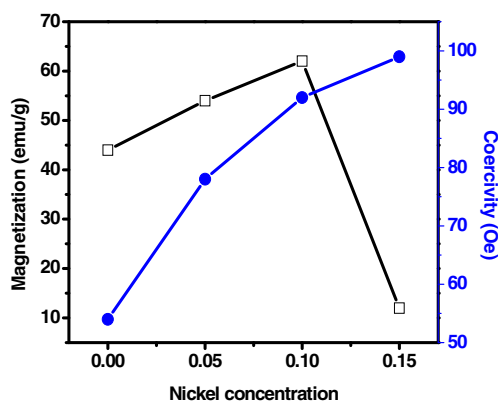
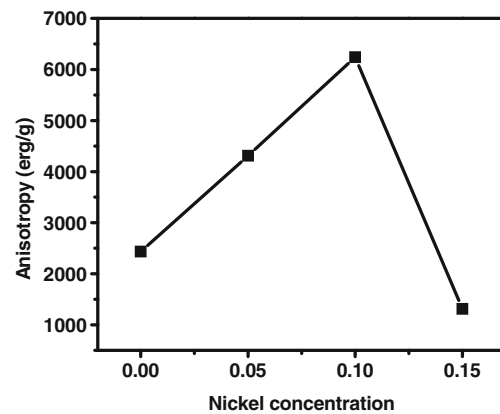
and therefore the magnitude of  $H_C$  also increases. The magnetic moment ( $n_B$ ) is calculated from the following formula [21]:

$$n_B = \frac{M \times M_s}{5588} \quad (9)$$

Where,  $M$  is molecular weight. The values of magnetic moments show that all the samples are ferromagnetic in nature.

### 3.6 Optical Analysis

The UV-Visible optical absorption spectra of nickel doped iron oxide  $\text{Ni}_x\text{Fe}_{3-x}\text{O}_4$  ( $x = 0, 0.05, 0.1, \text{ and } 0.15$ ) nanoparticles is shown in Fig. 14. The sample was prepared by dispersing the powder sample in 10 ml dimethyl fluoride (DMF) solution. First of all place a cuvette filled with DMF solution only to measure the intensity of light source at certain wavelength then place a cuvette filled with sample solution in the cell holder. The machine then recorded the light intensity and absorbance relative to the light intensity passes through solvent alone. The blue shift is observed in the absorption edge which is responsible for the quantum

**Fig. 12** Variation in magnetization and coercivity as a function of nickel concentration**Fig. 13** Variation in anisotropy as a function of nickel concentration

confinement and also the confirmation of the formation of nanoparticles.

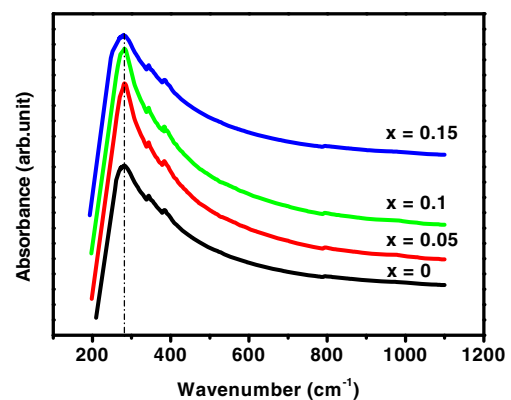
The absorption coefficient of all the samples are determined using the following equation [21]:

$$\alpha = \frac{4\pi k}{\lambda} \quad (10)$$

where  $\lambda$  is the wavelength in nanometer and  $k$  is the extension coefficient. The optical band gap energy is calculated by using Tauc relation [21]:

$$(\alpha h\nu)^n = c(h\nu - E_g) \quad (11)$$

where  $E_g$  is the optical band gap energy and  $h$  is the planks constant ( $6.62 \times 10^{-34}$ ) and  $c$  is a constant. The value of  $n$  for direct allowed, indirect allowed, direct forbidden and indirect forbidden transitions are 1/2, 2, 3/2 and 3, respectively. The optical band gap energy of all the samples is estimated by extrapolating straight line on  $x$ -axis which cuts the axis at some point, that point indicates the value of optical band gap energy. The graph of direct and indirect

**Fig. 14** UV-Visible absorption spectra of  $\text{Fe}_3\text{O}_4$ ,  $\text{Ni}_{0.05}\text{Fe}_{2.95}\text{O}_4$ ,  $\text{Ni}_{0.1}\text{Fe}_{2.9}\text{O}_4$ , and  $\text{Ni}_{0.15}\text{Fe}_{2.85}\text{O}_4$  nanoparticles



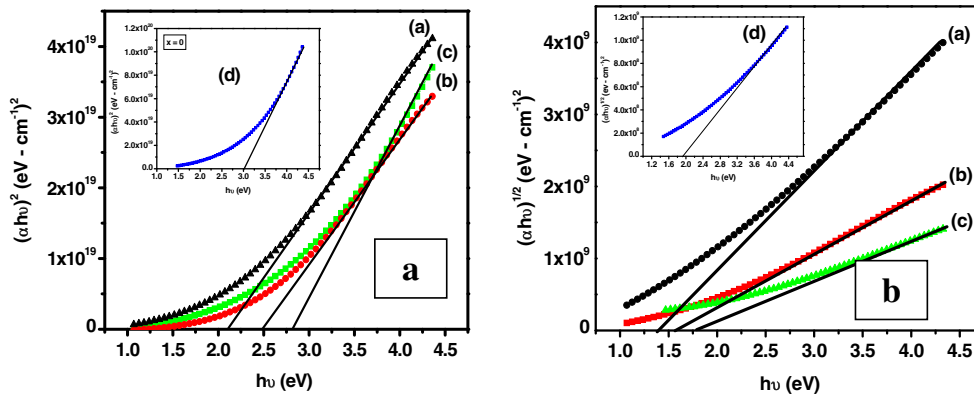


**Fig. 15** a Direct and b indirect band gap determination of  $Ni_xFe_{3-x}O_4$  ( $x = 0, 0.05, 0.1, \text{ and } 0.15$ ) nanoparticles

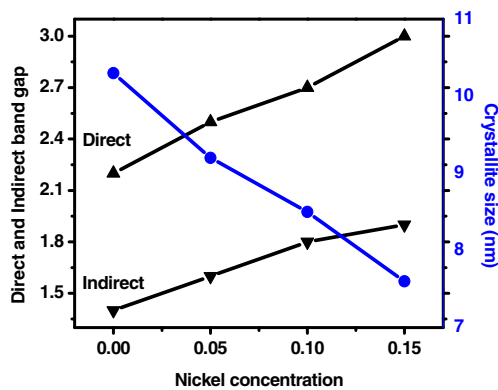


**Fig. 16** Variation in band gap energies and crystallite size as a function of nickel concentration

transition as a function of  $E_g$  for all the samples is plotted in Fig. 15a, b, respectively. It is revealed that when the concentration of nickel increases, the optical band gap energy increases. This may be due to the decrease in particle size as shown in Fig. 16.

When the crystallite size reaches to the nano scale where every element made up of only finite number of atoms, the electron hole pairs becomes very close together that the columbic force is no longer neglected and gives the overall higher kinetic energy. Hence, the larger band gap means that large energy is required to excite an electron from valance to conduction band. Optical band gap may also be increased because when the particle size decreases, the number of atoms becomes finite, the energy levels or overlapping orbital’s decreases, and the width of the band starts to narrow. This narrowing of the band results to increase in optical band gap. The values of optical band gap energy of direct and indirect transitions of all the samples have been tabulated in Table 7.

### 4 Conclusions

In the present study,  $Ni_xFe_{3-x}O_4$  ( $x = 0, 0.05, 0.1, 0.15$ ) nanoparticles have been successfully prepared using co-precipitation method. The structural characterization confirms that all the samples are composed of crystalline single phase inverse spinel structure. FTIR analysis confirms the single phase with the major band at 887  $cm^{-1}$ , which might be due to the stretching vibrations of metal-oxygen bond. SEM analysis reveals that the particles are spherical in shape with little agglomeration. The stability and the band gap values of nanoparticles have been increased with increasing nickel concentration. The values of magnetization, coercivity, and anisotropy increased with increasing nickel content in magnetite nanoparticles. Therefore, these particles may

**Table 7** Absorption and band gap values of all the samples

Samples	Absorption edge $\lambda$ (nm)	Direct band gap energy (eV)	Indirect band gap energy (eV)	Crystallite size (nm)
$Fe_3O_4$	281.78	2.2	1.4	10.3
$Ni_{0.05}Fe_{2.95}O_4$	279.98	2.5	1.6	9.2
$Ni_{0.10}Fe_{2.9}O_4$	276.41	2.7	1.8	8.5
$Ni_{0.15}Fe_{2.85}O_4$	273.47	3.0	1.9	7.6

be used in different biomedical applications such as in magnetic fluid hyperthermia etc.

## References

- Kang, Y., Zhou, L., Li, X., Yuan, J.: Cyclodextrin-modified hybrid magnetic nanoparticles for catalysis and adsorption. *J. Mater. Chem.* **21**(11), 3704–10 (2011)
- Barreto, C.H., Santiago, V.R., Freire, R.M., Mazzetto, S.E., Denardin, J.C., Mele, G., et al.: Magnetic nanosystem for cancer therapy using onocalyxone A, an antitumour secondary metabolite isolated from a Brazilian plant. *Int. J. Mol. Sci.* **14**(9), 18269–83 (2013)
- Czichos, H., Saito, T., Smith, L.E.: Springer handbook of metrology and testing. Springer, Berlin Heidelberg (2011)
- Schodek, D.L., Ferreira, P., Ashby, M.F.: Nanomaterials, nanotechnologies and design: an introduction for engineers and architects. Elsevier Science (2009)
- Fulekar, M.H.: Nanotechnology: importance and applications. I.K. International Publishing House (2010)
- Sahay, K., Shivendra Pathak K. S.: Basic concepts of electrical engineering. New Age International (P) Limited. Publishers (2006)
- Chen, C.W.: Magnetism and metallurgy of soft magnetic materials. Dover Publications (1977)
- Fuller, A.J.B.: Institution of electrical engineers. Ferrites at microwave frequencies. P. Peregrinus (1987)
- Pillai, S.O.: Modern physics and solid state physics (problems and solutions). New Age International (P) Limited (2008)
- Smallman, R.E., Bishop, R.J.: Modern physical metallurgy and materials engineering: science, process, applications. Butterworth-Heinemann (1999)
- Wei, Y., Han, B., Hu, X., Lin, Y., Wang, X., Deng, X.: Synthesis of Fe<sub>3</sub>O<sub>4</sub> nanoparticles and their magnetic properties. *Prod. Eng.* **27**, 632–7 (2012)
- Mart, I.-M.I., Espinosa, P.M.E., Rez HíR, P., Arenas-Alatorre, J.: Synthesis of magnetite (Fe<sub>3</sub>O<sub>4</sub>) nanoparticles without surfactants at room temperature. *Mater. Lett.* **61**(23GÇô24), 4447–51 (2007)
- Larumbe, S.: CG-PJIPLAG-PJAMLFGaDC, Ni doped Fe<sub>3</sub>O<sub>4</sub> magnetic nanoparticles. *Journal of nanoscience and nanotechnology* (2012)
- Suryanarayana, C.: Mechanical alloying and milling. CRC Press (2004)
- Trindade, T., da Silva, A.L.D.: Nanocomposite particles for bio-applications: materials and bio-interfaces. Pan Stanford (2011)
- Petcharoen, K., Sirivat, A.: Synthesis and characterization of magnetite nanoparticles via the chemical co-precipitation method. *Mater. Sci. Eng. B* **177**(5), 421–7 (2012)
- Nogi, K., Hosokawa, M., Naito, M., Yokoyama, T.: Nanoparticle technology handbook. Elsevier (2012)
- Rahman, O.U., Mohapatra, S.C., Ahmad, S.: Fe<sub>3</sub>O<sub>4</sub> inverse spinal super paramagnetic nanoparticles. *Mater. Chem. Phys.* **132**(1), 196–202 (2012)
- Akademia. S. R.: Chemical Society Russian Journal of Physical Chemistry. Chemical Society (2006)
- Patange, S.M., Shirsath, S.E., Jadhav, S.S., Jadhav, K.M.: Cation distribution study of nanocrystalline NiFe<sub>2–x</sub>Cr<sub>x</sub>O<sub>4</sub> ferrite by XRD, magnetization and Mossbuar spectroscopy. *Applications and material science* (2011)
- Fox, A.M.: Optical properties of solids. Oxford University Press (2001)